Available online at www.sciencedirect.com
ScienceDirect
Journal of Solid State Chemistry 180 (2007) 1489–1503
JOURNAL OF SOLID STATE CHEMISTRY
www.elsevier.com/locate/jssc

Oxygen nonstoichiometry and transport properties of strontium substituted lanthanum ferrite

Martin Søgaard*, Peter Vang Hendriksen, Mogens Mogensen

Fuel Cells and Solid State Chemistry Department, Risø National Laboratory, Frederiksborgvej 399, DK-4000 Roskilde, Denmark

Received 21 September 2006; received in revised form 2 February 2007; accepted 18 February 2007
Available online 28 February 2007

Abstract

This study presents an investigation of the properties of $(La_{0.6}Sr_{0.4})_{0.99}FeO_{3-\delta}$ (LSF40) covering thermomechanical properties, oxygen nonstoichiometry and electronic and ionic conductivity. Finally, oxygen permeation experiments have been carried out and the oxygen flux has been determined as a function of temperature and driving force.

The electrical conductivity was measured using a 4 probe method. It is shown that the electrical conductivity is a function of the charge carrier concentration only. The electron hole mobility is found to decrease with increasing charge carrier concentration in agreement with recent literature.

Values of the chemical diffusion coefficient, D_{Chem}, and the surface exchange coefficient, k_{Ex}, have been determined using electrical conductivity relaxation. At 800 °C D_{Chem} is determined to be $6.2 \times 10^{-6}\,cm^2\,s^{-1}$ with an activation energy of $137\,kJ\,mol^{-1}$. The surface exchange coefficient is found to decrease with decreasing oxygen partial pressure.

Oxygen permeation experiments were carried out. The flux through a membrane placed between air and wet hydrogen/nitrogen was $J_{O_2} \approx 1.8 \times 10^{-6}\,mol\,cm^{-2}\,s^{-1}$ (corresponding to an equivalent electrical current density of $670\,mA\,cm^{-2}$). The oxygen permeation measurements are successfully interpreted based on the oxygen nonstoichiometry data and the determined transport parameters.

Keywords: Oxygen ion diffusion; Strontium substituted lanthanum ferrite; Electrical conductivity relaxation; Oxygen nonstoichiometry; Thermal expansion; Oxide ion conductivity; LSF; Oxygen permeation; Perovskite

1. Introduction

Materials in the system $La_{1-x}Sr_xFeO_{3-\delta}$ (LSF) have in recent decades been investigated intensively. LSF has a perovskite structure. The perovskite materials have the general chemical formula ABO_3 where A is a large metal ion, typically a rare earth or alkaline earth metal, and B is a small cation, typically a transition metal. LSF exhibits high oxygen ion ($\sim 0.5\,S\,cm^{-1}$) and electronic conductivity ($\sim 100\,S\,cm^{-1}$) at 1000 °C. Furthermore, LSF can be stable in a reducing atmosphere and have good electro-catalytic properties for the reduction of oxygen. Due to these properties Sr substituted $LaFeO_{3-\delta}$ is interesting for application as cathode material in a solid oxide fuel cell (SOFC) and as a membrane material for the partial oxidation of methane.

The possible applications have led to detailed studies of the mechanical properties [1], defect chemistry [2–6], electronic transport properties [4,7–9] oxygen transport properties [10,11] and oxygen permeation [12] studies.

In each of the above-mentioned studies only a single or few material properties were studied and discussed. We believe that it is very valuable to measure all of these properties for one single composition prepared in one laboratory. The main motivation of this study is thus to investigate the properties of the system $(La_{0.6}Sr_{0.4})_{0.99}FeO_{3-\delta}$. We put special emphasis on relating the observed oxygen flux through a membrane with the oxygen nonstoichiometry, electronic and ionic conductivities and the catalytic properties.

We have studied the thermal expansion and the chemical expansion of the material. The oxygen nonstoichiometry has been measured as a function of the oxygen partial

*Corresponding author. Fax: +45 4677 5858.
E-mail address: martin.soegaard@risoe.dk (M. Søgaard).

0022-4596/$ - see front matter © 2007 Elsevier Inc. All rights reserved.
doi:10.1016/j.jssc.2007.02.012

pressure, p_{O_2}, and the temperature, T, using thermogravimetry. Electrical conductivity and electrical conductivity relaxation measurements have been carried out to determine the electronic and ionic transport parameters. Finally, the oxygen permeation through a membrane has been measured at different temperatures and p_{O_2}-gradients.

When giving a formula as $La_{0.6}Sr_{0.4}FeO_{3-\delta}$, it is tentatively assumed that no vacancies exist on the A- or B-site. This is incorrect due to simple thermodynamics and mainly because there will always be an uncertainty in the purity content and concentration/amount of the raw materials used for synthesizing the perovskite. From our own experience we find it challenging to synthesize a composition where $|1-[A]/([B]+[A])|<0.001$. If a small amount of excess iron oxides or cation vacancies inflicts physical properties such as the oxygen transport properties (chemical diffusion coefficient and surface exchange rate), it is imperative to know what excess component is present. We have therefore chosen to study the nominal composition $(La_{0.6}Sr_{0.4})_{0.99}FeO_{3-\delta}$ (LSF40). We are thus certain that we have an A-site deficient perovskite or that an iron rich compound is present in a small amount.

We have assumed that we have 1% cation vacancies on the A-site when analyzing our data. We compare our results with literature values given for the composition $La_{0.6}Sr_{0.4}FeO_{3-\delta}$ as this is the closest relevant composition given in the literature. We feel confident that properties such as the electrical conductivity, thermal expansion and defect chemistry will not be affected by the slight nonstoichiometry between the A- and B-site. The oxygen transport properties may of course be grossly effected by the nonstoichiometry between the A- and B-site [13]; however, in this study we know that we have an A-site deficient or iron rich perovskite. This gives us an advantage compared to other studies, where it is unknown if one has excess lanthanum/strontium or iron in the structure.

2. Theory

2.1. Defect model for $(La_{1-x}Sr_x)_sFeO_{3-\delta}$

Materials in the system $(La_{1-x}Sr_x)_sFeO_{3-\delta}$ can show large variations in oxygen stoichiometry. δ is the oxygen nonstoichiometry defined as $\delta = c_V V_M$, where c_V is the molar oxygen vacancy concentration and V_M is the molar volume. The oxygen stoichiometry in the $(La_{1-x}Sr_x)_sFeO_{3-\delta}$ system can be well described using a point defect model [5,6,8,10,14]. The point defects considered are given in Table 1 where the Kröger–Vink notation has been used. Lanthanum ferrite ($LaFeO_3$) is used as the reference composition.

Dissolution of $SrFeO_3$ in $LaFeO_3$ can be described as

$$SrFeO_3 \xrightarrow{LaFeO_3} Sr'_{La} + Fe^{\cdot}_{Fe} + 3O^{\times}_{O}. \quad (1)$$

The dissolution of $SrFeO_3$ results in the formation of $Fe^{\cdot}_{Fe}$. The defect equilibrium is established through the following two reactions:

$$V^{\cdot\cdot}_{O} + 2Fe^{\times}_{Fe} + \tfrac{1}{2}O_2 \rightleftharpoons O^{\times}_{O} + 2Fe^{\cdot}_{Fe}, \quad (2)$$

$$2Fe^{\times}_{Fe} \rightleftharpoons Fe^{\cdot}_{Fe} + Fe'_{Fe}. \quad (3)$$

Table 1
Point defects considered in $(La_{1-x}Sr_x)_sFeO_{3-\delta}$

A-site	B-site	O-site
$La^{\times}_{La}$ (La^{3+})	$Fe^{\times}_{Fe}$ (Fe^{3+})	$O^{\times}_{O}$ (O^{2-})
Sr'_{La} (Sr^{2+})	Fe'_{Fe} (Fe^{2+})	$V^{\cdot\cdot}_{O}$
V'''_{La}	$Fe^{\cdot}_{Fe}$ (Fe^{4+})	
	V'''_{Fe}	

Lanthanum ferrite ($LaFeO_3$) is used as reference for the Kröger–Vink notation. The chemical equivalent of the specie is given in parenthesis.

The first reaction is the oxygen incorporation into the perovskite matrix resulting in the annihilation of oxygen ion vacancies and the formation of tetravalent iron. The second reaction is a charge disproportionation reaction [8].

Wærnhus [5,6] suggested that a Schottky reaction also takes place in the $LaFeO_3$ system, at high oxygen partial pressures, $p_{O_2} > 10^{-7}$ atm:

$$\text{nil} \rightleftharpoons V'''_{La} + V'''_{Fe} + 3V^{\cdot\cdot}_{O}. \quad (4)$$

For the material considered here with 40% Sr doping on the A-site, the effect of the Schottky reaction is negligible as compared to the effect of the extrinsic defects and we have therefore neglected this reaction.

We have synthesized the nominal composition $(La_{0.6}Sr_{0.4})_{0.99}FeO_{3-\delta}$. We have assumed that the doping has resulted in the creation of 1% A-site vacancies instead of the composition $La_{0.6}Sr_{0.4}FeO_{3-\delta}$ with iron oxide particles included in a perovskite matrix. We thus have $[V'''_{La}] = 0.01$ and $[V'''_{Fe}] = 0$.

A number of conditions apply to the defect chemical equilibria. These include site restriction and charge neutrality. The A-site restriction gives

$$[La^{\times}_{La}] + [Sr'_{La}] + [V'''_{A}] = 1. \quad (5)$$

For B-site restriction,

$$[Fe'_{Fe}] + [Fe^{\times}_{Fe}] + [Fe^{\cdot}_{Fe}] + [V'''_{Fe}] = 1. \quad (6)$$

For O-site restriction,

$$[O^{\times}_{O}] + [V^{\cdot\cdot}_{O}] = 3. \quad (7)$$

And finally the electro-neutrality condition is

$$2[V^{\cdot\cdot}_{O}] + [Fe^{\cdot}_{Fe}] = [Fe'_{Fe}] + [Sr'_{La}] + 3[V'''_{La}] + 3[V'''_{Fe}]. \quad (8)$$

Insertion of the expressions for the chemical potential of ideally diluted defects into the equilibrium condition for reaction (2) and (3) gives the mass action-type equations:

$$\frac{[O^{\times}_{O}][Fe^{\cdot}_{Fe}]^2}{p_{O_2}[Fe^{\times}_{Fe}]^2[V^{\cdot\cdot}_{O}]} = K_{Ox}, \quad (9)$$

$$\frac{[Fe_{Fe}^{\cdot}][Fe_{Fe}^{\prime}]}{[Fe_{Fe}^{\times}]^2} = K_{Fe}, \tag{10}$$

where K_{Ox} and K_{Fe} are the equilibrium constants of the corresponding reactions.

2.2. Electrical conductivity relaxation

The sample used for electrical conductivity measurements had a well-defined rectangular bar shape with polished surfaces. Changes in the ambient p_{O_2} will change the electrical conductivity of the sample due to the new defect equilibrium. The change in electrical conductivity can, because of the well-defined geometry, be correlated to diffusion of oxygen ions in the samples. This method is henceforth referred to as electrical conductivity relaxation and is well described in the literature for obtaining oxygen transport properties [10,13,15–17]. According to Carslaw and Jaeger [18] the solution to the two-dimensional diffusion problem with a first order surface reaction can be described using the equation

$$\frac{\sigma(\infty)-\langle\sigma(t)\rangle}{\sigma(\infty)-\sigma(0)} = \sum_{n=1}^{\infty}\frac{2L_x^2\exp(-\beta_{n,x}^2 D_{Chem}t/l_x^2)}{\beta_{n,x}^2(\beta_{n,x}^2+L_x^2+L_x)} \times \sum_{n=1}^{\infty}\frac{2L_y^2\exp(-\beta_{n,y}^2 D_{Chem}t/l_y^2)}{\beta_{n,y}^2(\beta_{n,y}^2+L_y^2+L_y)}. \tag{11}$$

At time 0 the p_{O_2} around the sample is suddenly changed. $\sigma(\infty)$, σ_0 and $\langle\sigma_t\rangle$ are the electrical conductivities in the new equilibrium situation, at the time of the gas change and at time t, respectively. $L_x = l_x k_{Ex}/D_{Chem}$ and $\beta_{n,x}$ is the nth positive root to the equation $\beta_{n,x}\tan\beta_{n,x} = L_x$. k_{Ex} is defined from the equation $j_{Ex} = -k_{Ex}(C_{O^{2-}}(t)|_s - C_{O^{2-}}(\infty)|_s)$, where j_{Ex} is the flux of oxygen ions through the surface of the sample. $C_{O^{2-}}(\infty)|_s$ is the equilibrium concentration of oxygen ions (or vacancies) at the surface corresponding to the new p_{O_2}. $C_{O^{2-}}(t)|_s$ is the concentration of oxygen ions (or vacancies) at the surface at time t.

A two-dimensional solution is used since the conductivity is measured over a short distance in the center of a long sample [19]. The chemical diffusion coefficient and surface exchange coefficient have been determined by fitting Eq. (11) to the change in conductivity following an abrupt step in the ambient p_{O_2}. Further details on the fitting routine can be found in [20].

2.3. Oxygen permeation measurements

The oxygen permeation through membranes of $La_{1-x}Sr_xFeO_{3-\delta}$ system has been investigated in detail by tenElshof et al. [12] at high oxygen partial pressures $p_{O_2} > 10^{-3}$ atm where the electronic conductivity is high. In this study the membrane has been operated in mixtures of nitrogen and air ($p_{O_2} > 10^{-3}$ atm) and also under reducing conditions $p_{O_2} < 10^{-10}$ atm. In the latter regime the electronic transfer number is no longer close to unity. Therefore, it is necessary to use the ambipolar conductivity instead of the oxygen ion conductivity in order to describe the oxygen permeation precisely. Below, a summary is given of the equations used for describing the oxygen permeation through mixed ionic electronic conducting (MIEC) membranes. For further details on the oxygen permeation the reader is referred to [14,21–23].

The oxygen flux, J_{O_2}, through a membrane can be calculated using the Wagner equation:

$$J_{O_2} = \frac{RT}{4^2F^2L}\int_{\ln p''_{O_2,s}}^{\ln p'_{O_2,s}}\frac{\sigma_{el}\sigma_{O^{2-}}}{\sigma_{el}+\sigma_{O^{2-}}}\mathrm{d}\ln p_{O_2}, \tag{12}$$

where $\sigma_{O^{2-}}$ is the oxide ion conductivity, σ_{el} is the electronic conductivity, L is the thickness of the membrane, R is the universal gas constant and T is the absolute temperature. $p'_{O_2,s}$ is the oxygen partial pressure defined by the defect equilibrium at the surface of the membrane on the high-p_{O_2} side. $p''_{O_2,s}$ is the oxygen partial pressure defined by the defect equilibrium at the low-p_{O_2} side. Eq. (12) is valid through the entire p_{O_2}-range and is used when $p''_{O_2} < 10^{-10}$ atm when modelling the oxygen permeation measurements.

In the limits where the electronic conductivity is large ($\sigma_{O^{2-}} \ll \sigma_{el}$), Eq. (12) reduces to

$$J_{O_2} = \frac{RT}{4^2F^2L}\int_{\ln p''_{O_2,s}}^{\ln p'_{O_2,s}}\sigma_{O^{2-}}\mathrm{d}\ln p_{O_2}. \tag{13}$$

$\sigma_{O^{2-}}$ can be calculated using the Nernst–Einstein relationship [21]:

$$\sigma_{O^{2-}} = \frac{4F^2c_{O^{2-}}D_O}{RT} = \frac{4F^2[O_O^{\times}]D_O}{RTV_M} = \frac{4F^2[V_O^{\cdot\cdot}]D_V}{RTV_M}, \tag{14}$$

where D_O is the oxygen component diffusion coefficient and D_V is the vacancy diffusion coefficient. The equivalent electrical current density, i, corresponding to the oxygen flux through the membrane is

$$i = 4FJ_{O_2}. \tag{15}$$

Substituting Eqs. (15) and (14) into Eq. (13) we obtain:

$$i = \frac{D_V F}{V_M L}\int_{\ln p''_{O_2,s}}^{\ln p'_{O_2,s}}\delta\,\mathrm{d}\ln p_{O_2}. \tag{16}$$

Here, we have assumed that D_V is independent of $[V_O^{\cdot\cdot}]$. Notice, that Eq. (15) is an approximation only valid when $p''_{O_2} > 10^{-5}$, when the electronic conductivity is much higher than the ionic conductivity.

The driving force for the surface exchange reaction is the difference in the chemical potential of oxygen across the surface. Assuming linear electrode kinetics for the surface exchange reaction, the current density is proportional with the overpotential, η. η can thus be expressed from the oxygen concentration in the gas phase and the oxygen concentration defined by the defect equilibrium in the

surface of the MIEC, $p'_{O_2,s}$. This gives

$$\eta_{cat} = ir_{cat} = \frac{RT}{4F}\ln\left(\frac{p'_{O_2}}{p'_{O_2,s}}\right), \quad (17)$$

$$\eta_{an} = ir_{an} = -\frac{RT}{4F}\ln\left(\frac{p''_{O_2}}{p''_{O_2,s}}\right), \quad (18)$$

where, r_{cat} and r_{an} are the area-specific equivalent resistance describing the cathode and anode reaction, respectively. The area-specific resistance of the interface region can be calculated from the surface exchange coefficient, k_O, measured in a nongradient driven experiment such as a $^{16}O/^{18}O$ tracer diffusion experiment, using the relation [24]:

$$r = \frac{RT}{4F^2 c_O(p_{O_{2,s}})k_O(p_{O_{2,s}})}\frac{1}{}. \quad (19)$$

k_O can be related to the surface exchange coefficient, k_{Ex}, measured in a gradient driven experiment such as in electrical conductivity relaxation using the relation $k_O = k_{Ex}/\gamma$ [10]. $\gamma = 1/2t_{el}\partial \ln p_{O_2}/\partial \ln c_O$ where c_O is the concentration of oxygen ions [21]. Hendriksen et al. [22] have given an algorithm to solve the bulk permeation combined with the surface exchange reactions. In this way, knowing the defect chemical equilibrium and the transport parameters, prediction of the flux through the membrane is possible.

3. Experimental

We have used the glycine–nitrate route to prepare LSF40 [25]. Stock solutions were prepared by dissolving the nitrates of the metal ion in distilled water ($\rho_{Res} = 18.2\,M\Omega\,cm$). All the raw materials had a purity of 99.9% or better. The concentration of the metal nitrate solutions was carefully determined by thermogravimetry. The nitrate solutions were mixed in the correct stoichiometric amount and glycine was added, such that the stoichiometric amount of glycine to that of the stoichiometric amount of the nitrates was 0.548. When the nitrate and glycine react, it takes place according to the reaction [26]

$$\frac{9}{x}M(NO_3)_x + 5NH_2CH_2COOH \rightarrow 10CO_2 + 7N_2 + \frac{25}{2}H_2O + \frac{9}{x}MO_{x/2}, \quad (20)$$

where M is a metal ion. The reaction is very exothermic but the heat of evaporation of water consumes a lot of the released energy ensuring a controlled reaction. The glycine–nitrate route gives a uniform powder with a small grain size ($\ll 1\mu m$). The powder obtained from the synthesis was calcined at 900 °C for 24 h in order to obtain a single phase material with a uniform cation distribution. The calcined powder was ball milled in ethanol for 24 h. Samples of the perovskites were prepared by using polyvinyl alcohol (PVA) ($MW = 100.000\,g\,mol^{-1}$) as binder. Samples were pressed uniaxially followed by isostatic pressing at 325 MPa. Samples were sintered at 1200 °C for 4 h and at 1150 °C for 16 h and slowly cooled in order to avoid fragile ceramics. The samples for dilatometry, thermogravimetry, electrical conductivity and electrical conductivity relaxation measurements were prepared using the above method.

Due to problems in obtaining dense samples of LSF40, powders were also prepared by a modified Pechini route [27]. The sample for the oxygen permeation experiment was thus prepared by mixing the aqueous nitrate solutions in the correct stoichiometric ratio. The total amount of cations in mole is designated by N_j. $4N_j$ citric acid was added to the solution. The solution was heated to 80−90 °C and $2N_j$ polyethylene glycol ($MW = 200\,g\,mol^{-1}$) (PEG 200) was added to the solution. The solution was heated to the boiling point on a hot plate for several hours until no further reaction could be observed. The powder was further heated to 300 °C in a furnace. Subsequently, the powder was removed from the beaker and precalcined at 600 °C for 12 h and crushed and calcined at 1000 °C for 12 h. The preparation with pressing and sintering was carried out in the same way as with the powder from the glycine–nitrate method.

Phase purity and lattice parameters of the compositions were determined using a Stoe Bragg–Brentano X-ray diffractometer with Cu_{K_α} radiation.

The dilatometry measurements were carried out in a Netzsch 402C dilatometer. A sample of Al_2O_3 was tested on the equipment prior to use. The expansion curve of Al_2O_3 upon heating was within 4% similar to literature data.

The density of the sample used for dilatometry was $\rho = 5.82\,g\,cm^{-3}$ which corresponds to 94% of the density determined from X-ray diffraction (XRD). Table 2 shows the experimental program to which the sample was subjected. At oxygen partial pressures lower than $p_{O_2} < 8.84 \times 10^{-11}$ atm the sample contracted with decreasing p_{O_2}. This is attributed to degradation or sintering of the sample. No measurements with physical meaning could be obtained in this region. When the sample was removed from the dilatometer, it seemed intact; however, the sample was fragile and small pieces fell off upon removal from the equipment. The sample holder in the dilatometer had turned reddish (Fe_2O_3) indicating evaporation of iron.

A sintered pellet of LSF40 was crushed and used for the thermogravimetry measurements (Seiko TG/DTA 320U).

Table 2
Experimental conditions during the dilatometry experiment

T_{Start} (°C)	T_{End} (°C)	Rate (°C min^{-1})	p_{O_2} (atm)
20	1000	1	0.209
1000	1000		0.209
1000	1000		1.10×10^{-3}
1000	1000		8.84×10^{-11}

At 800, 900, 1000, 1100 and 1200 °C (±2 °C) the oxygen partial pressure over the sample was varied using mixtures of nitrogen and air (10^{-4} atm $< p_{O_2} <$ 0.209 atm). The total flow over the sample was 300 ml min^{-1} (standard temperature and pressure (STP)) and was controlled using Brooks 5850s flow controllers. The p_{O_2} was measured downstream from the thermogravimetric analyzer using a zirconia oxygen sensor. Following the measurements in nitrogen/air, the p_{O_2} was varied using carbon dioxide and 9% hydrogen in nitrogen at 900, 1000, 1100 and 1200 °C. These mixtures give oxygen partial pressures below 10^{-5} atm. After thermogravimetry the phase purity was investigated again using XRD. A hexagonal perovskite phase with very high crystallinity was found.

A rectangular bar with dimensions 0.149 cm × 0.147 cm × 1.716 cm, to be used for the conductivity relaxation measurements, was cut from a larger sintered sample. The bar was very fragile and therefore only polished with SiC-paper #1000. The density of the sample was 92% of the density determined from XRD. The electrical conductivity of the sample was measured using a 4 probe technique. A current of 10 mA was applied through the sample and the voltage drop was measured over a well-defined distance (0.5 cm) in the center of the sample. The sample was placed in a quartz tube in which the atmosphere could be changed rapidly (< 10 s). After heating to the desired temperature, the oxygen partial pressure was changed by varying the flow rates of nitrogen and air. The flows of nitrogen and air were controlled using Brooks flow controllers. The total flow was kept constant at 250 ml min^{-1} (STP).

Fig. 1 shows a schematic of the equipment used for the oxygen permeation experiment. The studied membrane had a thickness of 1.34 mm and a diameter of 15.3 mm. The sample was 95% dense (geometrical density) when compared to the density determined from XRD. The membrane was polished thoroughly with SiC-paper #1000 followed by 6 μm diamonds and finally an SiO_2 suspension. The membrane was placed between two alumina tubes with an inner diameter of 10.25 mm. Between the alumina tube and the membrane, a gold ring is placed on both sides (200 μm thickness) for sealing. The area exposed to the gases is therefore approximately 0.825 cm^2. A second alumina tube is placed within the outer alumina tube providing a gas outlet. It terminates approximately 1 mm above the membrane. A thermocouple is placed within the inner alumina tube such that it is close to the membrane (< 1 mm). The gas is blown in via the space between the outer and inner alumina tube and the gas exits via the inner alumina tube. This arrangement ensures that no stagnant gas layer is present close to the membrane. The setup is placed in the hot zone of a 40 cm long tube furnace. The membrane was heated to 1000 °C. The sealings between the alumina tubes and the membrane were observed to be gas tight after 24 h.

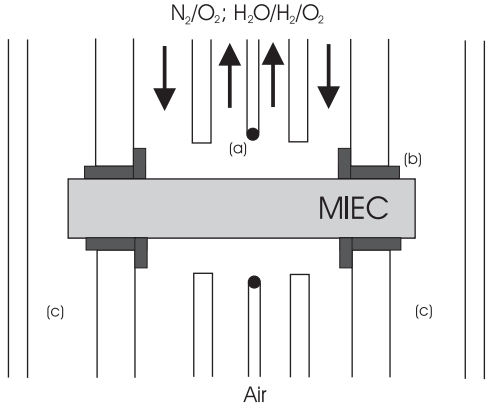

Fig. 1. Schematic of setup used for the oxygen permeation measurements. (a) Thermocouple; (b) gold seals; (c) sweep gas compartment. The arrows indicate the flow direction. A similar flow pattern applies for the air side.

In all the experiments air was fed to one side of the membrane with a flow of approximately 100 ml min^{-1} (STP). The other side of the membrane was first exposed to different mixtures of nitrogen and air ($p_{O_2} > 10^{-5}$ atm) at 1000 and 850 °C. The oxygen partial pressure was measured upstream and downstream of the membrane. The increased oxygen content in the gas (downstream of the membrane) is assumed to originate from the oxygen permeation through the membrane. Knowing the flow rate of the gas, the oxygen permeation through the membrane can be calculated. The oxygen flux has been corrected due to edge effects according to the procedure described by Crank [28]. The correction is $F_0/F = 0.919$, where F is the measured permeation and F_0 is the permeation without edge effects.

When the flux had been measured with nitrogen/air mixtures on the low-p_{O_2} side, the anode gas was shifted to wet hydrogen/nitrogen mixtures. The oxygen permeation is in this case calculated from the increase in the oxygen partial pressure and the increase in water content. Oxygen permeation experiments were carried out in the temperature range of 500–1000 °C.

4. Results and discussion

4.1. Structure

All reflections in the XRD pattern of a dense membrane of LSF40 could be assigned to a hexagonal perovskite phase, with space group $R\bar{3}c$. The lattice constants were determined to $a_h = 5.530$, $c_h = 13.426$. The results obtained in this study are in agreement with literature values, e.g. Dann et al. [29] and Menon et al. in [30].

4.2. Dilatometry

Fig. 2 shows the relative change in length upon heating (left axis) for LSF40. The thermal expansion coefficient, α, defined as $\alpha = 1/l\partial l/\partial T$ is shown on the right axis. At 100 °C, $\alpha = 11.2 \times 10^{-6}$ K^{-1} which increases to 14.0×10^{-6} K^{-1} at 600 °C. For $T > 600$ °C the thermal expansion coefficient increases from 14.0×10^{-6} to 23.8×10^{-6} K^{-1}. This is attributed to chemical expansion caused by the loss

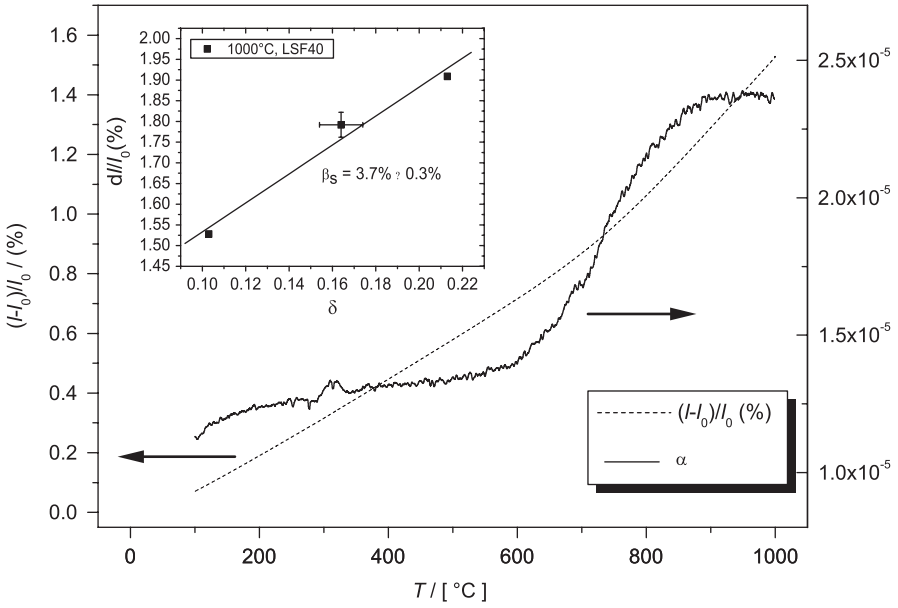

Fig. 2. Relative length (in percent, left axis) as a function of the temperature. Also shown is the linear thermal expansion coefficient, α (right axis). In the inset is shown the change in relative length (in percent) as a function of the oxygen nonstoichiometry at 1000 °C. The line shows the best linear fit to the relative length as a function of the oxygen nonstoichiometry. The value of the chemical expansion coefficient, β_s, is depicted in the figure. The error bars are shown for one point and the magnitude is representative for the remaining points.

of oxygen from the lattice [31]. The integral thermal expansion coefficient, α_{int}, defined as

$$\alpha_{int} = \frac{\int_{T_0}^{T_1} \alpha(T)\,dT}{T_1 - T_0} \tag{21}$$

has, in the temperature range of 100−600 °C, been calculated to $\alpha_{int} = 12.9 \times 10^{-6}\,K^{-1}$. Fossdal measured the thermal expansion coefficient for $La_{0.6}Sr_{0.4}FeO_{3-\delta}$ using dilatometry [32]. In the temperature range $RT < T < 600$ °C a value of $(13.4 \pm 0.4) \times 10^{-6}\,K^{-1}$ was found. In the temperature range 600 °C $< T <$ 1000 °C values in the range 13.4×10^{-6}−$(25.7 \pm 0.6) \times 10^{-6}\,K^{-1}$ were obtained. The values in Fig. 2 are thus in good agreement with the values measured by Fossdal. Fossdal et al. [32] also found that $La_{0.6}Sr_{0.4}FeO_{3-\delta}$ undergoes a phase transition from rhombohedral to cubic at 850 ± 50 °C. Adler found a value of $\alpha_{int} = 15.4 \times 10^{-6}\,K^{-1}$ for the composition $La_{0.6}Sr_{0.4}Co_{0.2}Fe_{0.8}O_{3-\delta}$ in the temperature range 100 °C $< T <$ 600 °C [31]. The addition of Co thus increases the thermal expansion coefficient. In the temperature range of 100−1000 °C the integral thermal expansion coefficient has been calculated to $\alpha_{int} = 16.2 \times 10^{-6}\,K^{-1}$ for LSF40. It is also observed from Fig. 2 that α becomes constant in the range 850 °C $< T <$ 1000 °C. Assuming constant values of the thermal and chemical expansion coefficient, this must indicate that $\partial\delta/\partial T$ is constant, cf. Eq. (22) below.

In order to analyze the chemical expansion further, the inset in Fig. 2 shows $(l - l_0)/l_0$ (l_0 is the sample length at RT) as a function of the oxygen nonstoichiometry. The data were obtained by changing the p_{O_2} around the sample. Only three points were valid to include in the graph, air ($p_{O_2} = 0.209$ atm), CO_2 ($p_{O_2} = 1.1 \times 10^{-3}$ atm) and one mixture of CO_2 and H_2 ($p_{O_2} = 8.8 \times 10^{-11}$ atm). The oxygen partial pressures have been converted to values of δ using oxygen nonstoichiometry data (presented in Section 4.3). The chemical expansion coefficient, β_s, defined as

$$\frac{l - l_0}{l_0} = \beta_s \delta \tag{22}$$

has been calculated to 3.7 ± 0.3% from the data depicted in Fig. 2. This can be compared to a value of 2.4 ± 0.5% for $(La_{0.6}Sr_{0.4})_{0.99}\,CoO_{3-\delta}$ [33]. Thus, it can be concluded that $(La,Sr)FeO_{3-\delta}$ perovskites expand more on reduction than $(La,Sr)CoO_{3-\delta}$ perovskites for the same changes in δ.

4.3. Oxygen nonstoichiometry from thermogravimetry

Fig. 3 shows the oxygen nonstoichiometry as a function of $\log(p_{O_2})$ at different temperatures. The clearly observed plateau is assumed to correspond to electronic stoichiometry $([Sr'_{La}] + 3[V'''_A])/2$ and has been used as reference point for the determination of the absolute oxygen content in the material. This plateau could be determined with very high accuracy (δ was within the range ±0.001) at 900 °C. We have not observed iron oxides in the material and from the amount of material used in the synthesis up to 1% cation vacancies may have formed on the A-sites. From studies by Waernhus we are, however, skeptical regarding the formation of such large concentrations of A-site vacancies, since these only form to a very small extent in $LaFeO_3$ [5,6]. If one assumes that iron oxides form instead of A-site cation vacancies, the oxygen nonstoichiometry

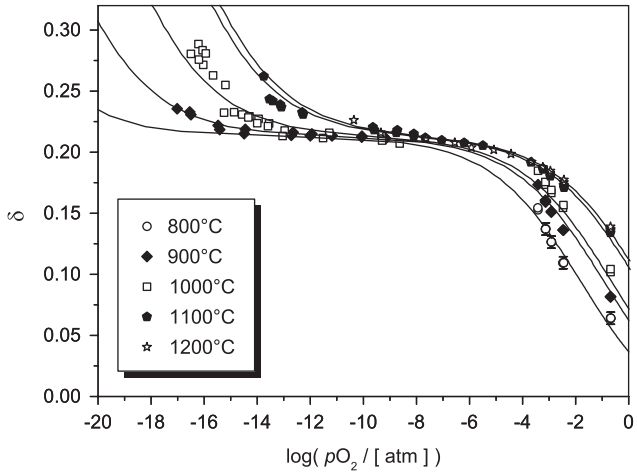

Fig. 3. Oxygen ion vacancy concentration as a function of $\log(p_{O_2})$. The solid lines show the best fit to the point defect model presented in Section 2.1. The maximum value of the error is shown for $T = 800\,^{\circ}C$.

curves should be shifted downwards such that the plateau is at a vacancy concentration of $\delta = 0.20$. We have therefore estimated the uncertainty of the measured values of δ on the absolute scale to be ± 0.015, whereas relative changes in δ with changing p_{O_2} at one temperature are determined with an uncertainty better than ± 0.005. When lowering the p_{O_2} (at a constant temperature) or increasing the temperature (at a constant p_{O_2}), the oxygen vacancy concentration increases. The solid lines represent the best fit using the point defect model described in Section 2.1. Values of K_{Ox} and K_{Fe} are given in Table 3.

Expressing the changes in standard Gibbs free energy, standard enthalpy and standard entropy for each of the reactions i (reaction (2) and (3)) we get the relationship

$$RT \ln K_i = -\Delta G_i^0 = -\Delta H_i^0 + T\Delta S_i^0. \quad (23)$$

Values of ΔH_i and ΔS_i have thus been determined by plotting $\ln(K_i)$ against $1/T$. The slope gives $-\Delta H_i^0/R$ and the intercept with the second axis gives ΔS_i^0. The values of the enthalpy and entropy changes of the reactions are compared to values reported by Mizusaki et al. [2] in Table 4. The values measured in this study are observed to be in good agreement with the values by Mizusaki et al.

It should be noted that the point defect model is observed to fit well at 1100 and 1200 °C. However, for 1000, 900 and 800 °C a slight deviation between the point defect model and the measured data is observed.

Fig. 4 shows the thermodynamic enhancement factor defined as $1/2t_{el}(\partial \ln p_{O_2})/(\partial \ln c_O)$ where c_O is the concentration of oxygen ions [21]. t_{el} is the electronic transference number and has been calculated from electrical conductivity measurements presented in Section 4.4. t_{el} is approximately 0.6–0.8 in the region $10^{-10}\,\text{atm} < p_{O_2} < 10^{-15}\,\text{atm}$, but for $p_{O_2} > 10^{-4}\,\text{atm}$, $t_{el} > 0.99$. For $0.209\,\text{atm} > p_{O_2} > 10^{-4}$ atm the value of γ is approximately 100 for $T =$ 900 and 1000 °C. The inset shows γ in the entire measured p_{O_2}-range as calculated from the point defect model at 1000 °C. Also shown is the actual measured value of γ obtained from a third degree polynomial fit to the measured data. γ becomes large (~1000) at 1000 °C in the range $10^{-13}\,\text{atm} < p_{O_2} < 10^{-7}\,\text{atm}$. In this region changes in the p_{O_2} do not lead to significant changes in the oxygen nonstoichiometry, thereby resulting in a large value of γ. Evidently, from the inset a slight deviation between the values of γ deduced from the polynomial fit to the oxygen nonstoichiometry measurements and the value deduced from the point defect model is observed. In order to obtain more precise values of the oxygen transport properties, we have used the polynomial fit curves as these represent the variation of δ with p_{O_2} better than the point defect model.

Table 3
Equilibrium constants determined by fitting the model described in Section 2.1 to the measured data

T (°C)	K_{Ox} (atm$^{1/2}$)	K_{Fe}
800	4.2×10^{-2}	6.32×10^{-7}
900	1.15×10^{-1}	2.31×10^{-6}
1000	1.59×10^{-1}	7.73×10^{-6}
1100	4.96×10^{-1}	1.60×10^{-5}
1200	6.10×10^{-1}	1.73×10^{-5}

Table 4
Standard enthalpy and entropy changes for the reactions presented in the theory section. Values in parenthesis are from Mizusaki et al. [2] for $La_{0.6}Sr_{0.4}FeO_{3-\delta}$

	Redox reaction	Disproportionation reaction
ΔH^0 (kJ mol^{-1})	90.0 ± 9.5 (97.5)	114.8 ± 13.4 (120.0)
ΔS^0 (J mol^{-1} K)	57.7 ± 7.6 (67.7)	-10.2 ± 10.8 (−4.7)

4.4. Electrical conductivity of LSF40

Fig. 5 shows the electrical conductivity of LSF40 as a function of $\log(p_{O_2})$. A *pn*-transition is observed at 1000 °C in the p_{O_2}-range of $10^{-10}-10^{-14}$atm. At 900 °C the *pn*-transition has moved to lower p_{O_2}approximately in the range of $10^{-12}-10^{-16}$ atm. From the *pn*-transition at 900 and 1000 °C, the value of the electronic band gap, E_g, can be calculated. Extrapolating the *p*- and *n*-type conductivities, one determines a minimum value of the electronic conductivity σ_{min}. This has been done for the temperatures 1000 and 900 °C. When calculating the band gap it is assumed that the mobility of the electrons, μ_n, equals the mobility of the electron holes, μ_p, and that the mobilities are independent of the temperature. At the minimum conductivity $n = p$ and under the assumption $\mu_n = \mu_p$ it follows that $\sigma_{min} = 2n\mu_n e = 2p\mu_p e$. The band gap can then be calculated using the relation $n = p = \sqrt{N_C N_V}\exp(-E_g/2k_BT)$ [34], where $N_{C,V}$ is the effective density of states of the electrons/holes in the conduction and valence bands which equals $N_{C,V} = 2(2\pi m^*_{e,h} k_B T/h^2)^{3/2}$, k_B is the

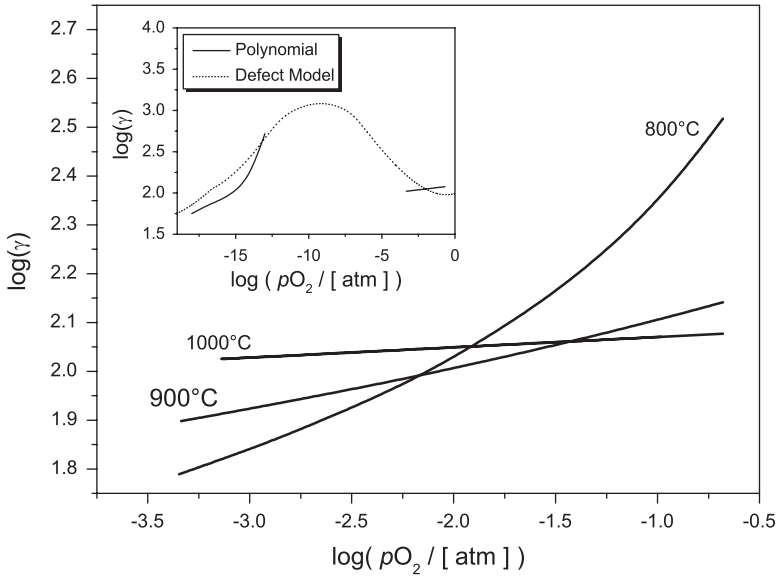

Fig. 4. Thermodynamic enhancement factor of LSF40 at 1000, 900 and 800 °C. γ is defined as $1/2\,t_{el}\,(\partial \ln p_{O_2})/(\partial \ln c_O)$. The curves have been calculated by fitting a third degree polynomial to the oxygen nonstoichiometry data. The solid line in the inset shows the measured value of γ as a function of $\log(p_{O_2})$ at 1000 °C in the entire measured p_{O_2}-range. The dotted line is calculated using the point defect model.

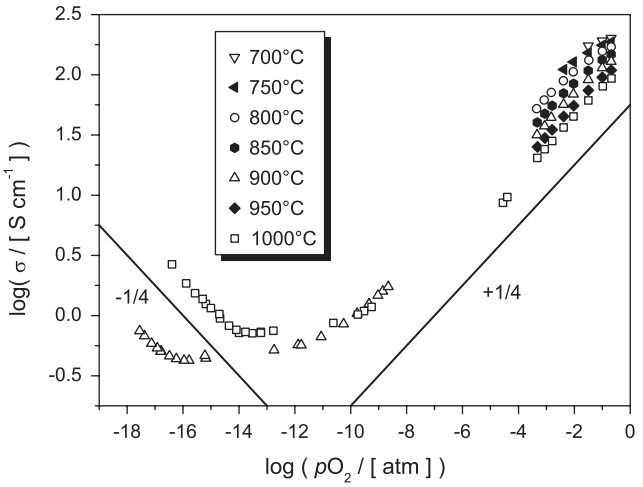

Fig. 5. Electrical conductivity as a function of $\log(p_{O_2})$. The solid lines indicate the slopes $+\frac{1}{4}$ and $-\frac{1}{4}$.

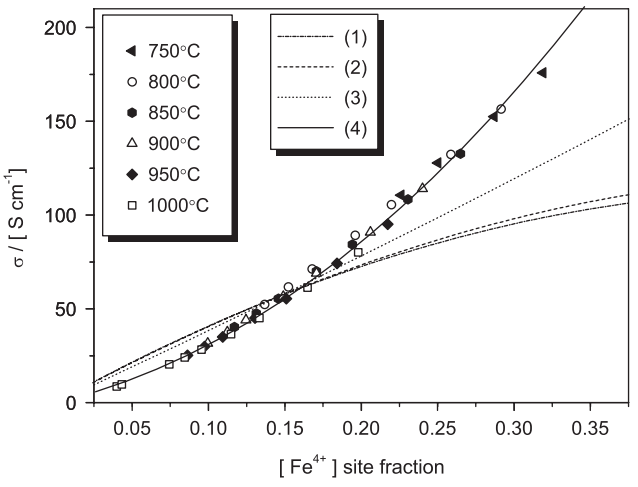

Fig. 6. Electrical conductivity as a function of $[Fe^{4+}]$ for data recorded with $p_{O_2} > 10^{-5}$ atm. The lines indicate fits to the models presented in Section 4.4.

Boltzmann constant, h is the Planck constant and $m^*_{e,h}$ is the effective mass of the electron/electron hole. In this case $m^*_{e,h}$ has been set equal to the electron mass. In this way the band gap has been calculated to $E_g = 1.4$ eV. However, the uncertainty is estimated to be approximately 0.7 eV. It should be noted that the band gap in this study has been calculated on the basis of a slope determined from two points, and therefore has such a large uncertainty.

In order to see if the electrical conductivity can be described as a small polaron type, Fig. 6 shows the electrical conductivity as a function of the site fraction of tetravalent iron (calculated from the oxygen nonstoichiometry data). In the calculation it is assumed that the remaining iron is trivalent.

From Fig. 6 it must be concluded that within the uncertainty the electrical conductivity in the p-type region is independent of the temperature and only depends on the charge carrier concentration. A similar result was also found by Patrakeev [4]. It should be noted that the slight upward curvature of the $\sigma - [Fe^{4+}]$ curve is indicative of a mobility that varies with the charge carrier concentration. The lack of thermal activation of the electrical conduction (or even decreasing electrical conductivity with the temperature at a constant charge carrier concentration) is surprising since LSF is generally considered as a small polaron conductor [8].

Values of the electron–hole mobility measured in this study have been calculated as $\mu_p = \sigma/(N_{ABO_3} e[Fe^{4+}])$,

where N_{ABO_3} is the number of ABO_3 formula units pr. cm^3. The values of the electron–hole mobility vary in the range of $0.2\,cm^2V^{-1}s^{-1}$ ($\delta = 0.06$)–$0.1\,cm^2V^{-1}\,s^{-1}$ ($\delta = 0.16$) (the electron–hole mobility decreases linearly with decreasing oxygen content). The electron–hole mobility values calculated in this study are in very good agreement with values measured by Patrakeev for the composition $La_{0.5}Sr_{0.5}FeO_{3-\delta}$ [4].

The lines in Fig. 6 are best fit to the equation $\sigma = \mu_p(N_{ABO_3}e[Fe^{4+}])$. Several models have been investigated where the variation between the models lies in μ_p and how this may be affected by considering variations on available sites for the electron hole to jump to. The models are described henceforth:

1. The mobility is assumed proportional to $[Fe_{Fe}^{\times}]$. In order for an electron hole to jump to the next site, the next site should be an $[Fe_{Fe}^{\times}]$-ion.
2. The mobility is assumed proportional to $[Fe_{Fe}^{\times}][O_O^{\times}]$. In order for an electron hole to jump to the next site, there should be an oxygen ion in between the two sites (and not an oxygen vacancy) and the next site should be an $[Fe_{Fe}^{\times}]$ ion.
3. The mobility is assumed proportional to $[Fe_{Fe}^{\times}(\text{free})][O_O^{\times}]$ where $[Fe_{Fe}^{\times}(\text{free})] = [Fe_{Fe}^{\times}] - 2\delta$. This corresponds to one oxygen vacancy blocks two $Fe_{Fe}^{\times}$ sites. And further there should be an oxygen ion between the two sites.
4. The mobility is assumed proportional to $[Fe_{Fe}^{\times}(\text{free})][O_O^{\times}]$ where $[Fe_{Fe}^{\times}(\text{free})] = [Fe_{Fe}^{\times}] - n\delta$, where n is a fitting parameter. This correspond to one oxygen vacancy blocks n $Fe_{Fe}^{\times}$sites. And further there should be an oxygen ion between the two sites. The solid line in the figure corresponds to model 4, where $n = 3.9$.

From Fig. 6 it is observed that both models 1 and 2 (corresponding to a simple available site correction on the mobility) show a curvature which is inconsistent compared to the measured data. Model 3 has a correct curvature, however, not large enough. In model 4 where the fitting parameter n has been introduced, the model describes the observed data with good accuracy. The electrical conductivity can thus be described assuming that each vacancy "eliminates" 3.9 $Fe_{Fe}^{\times}$ sites resulting in reduced mobility.

4.5. Oxygen diffusion

Fig. 7 shows the values of D_{Chem} deduced from the transient response in conductivity to a step in p_{O_2} as explained in Section 2.2. The values of D_{Chem} are taken from reduction steps and are plotted as a function of the final p_{O_2}. For $p_{O_2} < 0.001$ atm the uncertainty on D_{Chem} becomes large. For $p_{O_2} < 0.001$ atm oxygen incorporation into the sample is governed by the surface exchange reaction and thus, it becomes very difficult to measure D_{Chem} as illustrated with the large error bars. D_{Chem} is observed to be fairly constant in the region $T > 850\,^{\circ}C$ and $p_{O_2} > 0.005$ atm. At lower temperatures D_{Chem} seems to decrease with decreasing p_{O_2}. The dashed lines are a calculation of the chemical diffusion coefficient using the oxygen nonstoichiometry data (third degree polynomial fit to the $\delta - \log(p_{O_2})$ measurements) and the assumption of a constant vacancy diffusion coefficient. We have used that $D_V c_V = D_O c_O$ and $D_{Chem} = \gamma D_O$, where D_O is the oxygen component diffusion coefficient. The values of the vacancy diffusion coefficient that have been used to calculate the dashed lines in Fig. 7 are presented in Table 5.

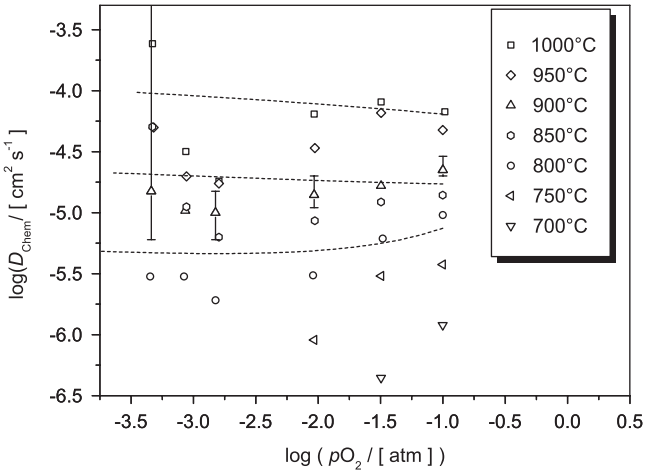

Fig. 7. $\log D_{Chem} - \log(p_{O_2})$ diagram for LSF40 as a function of the temperature. The error bars are shown for 900 °C and are typical for the remaining temperatures. The dashed lines represent a calculation of the chemical diffusion coefficient at 800, 900 and 1000 °C using the oxygen nonstoichiometry data and the assumption of a constant vacancy diffusion coefficient. The values of the vacancy diffusion coefficients are displayed in Table 5.

Table 5
Values of D_V used to calculate the dashed lines in Fig. 7

T (°C)	D_V ($cm^2\,s^{-1}$)
800	1.46×10^{-6}
900	4.37×10^{-6}
1000	1.41×10^{-5}

The decrease in D_{Chem} with decreasing p_{O_2} for $T < 850\,^{\circ}C$ is due to a decreasing thermodynamic factor according to Fig. 4. The increasing (or nearly constant) value of D_{Chem} with decreasing p_{O_2} for $T > 850\,^{\circ}C$ is due to an almost constant value of the thermodynamic factor, but an increasing oxygen vacancy concentration.

At 750 and 700 °C it was not possible to measure oxygen transport properties at $p_{O_2} < 0.01$ atm since the oxygen exchange became very slow (relaxation times > 24 h).

The measured values of D_{Chem} have been converted to a vacancy diffusion coefficient. Values of D_V are shown in Fig. 8, but only for the temperatures 800, 900 and 1000 °C, where the thermodynamic enhancement factor can be calculated accurately on the basis of the oxygen nonstoichiometry data. The vacancy diffusion coefficient is determined less accurately than the chemical diffusion

coefficient due to the uncertainty on the absolute value of the oxygen nonstoichiometry (±0.015). For $p_{O_2} > 0.008$ atm D_V is observed to be fairly constant and the activation energy (average of the three measurements at each temperature) has been calculated to $E_A = 129 \pm 9\,kJ\,mol^{-1}$. A slight decrease in D_V might be observed; however, the effect is masked by the uncertainty. If a decrease in D_V is present, it would indicate that the mobility of the vacancies decreases with increasing oxygen nonstoichiometry.

Values of the oxygen ion transport parameters of $La_{0.6}Sr_{0.4}FeO_{3-\delta}$ have been measured by Ishigaki [35] and tenElshof et al. [10,12]. These values are shown in Table 6 and compared with values obtained in this study. The values measured in this study seem in general slightly lower (by approximately 50%) than the literature values. In Refs. [10,12] it is only specified that the density exceeds 92% of the theoretical value, which is the same as in this study. In Ref. [35] single crystals of $La_{0.6}Sr_{0.4}FeO_{3-\delta}$ were used; however, only little detail was given on the fabrication and phase purity of the material.

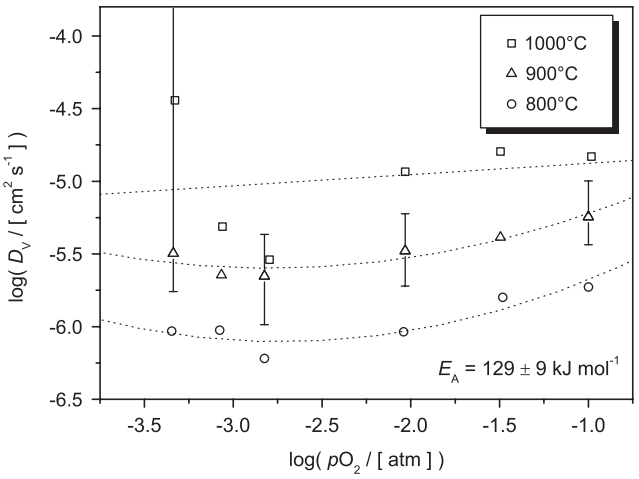

Fig. 8. $\log D_V$–$\log(p_{O_2})$ diagram for LSF40 as a function of the temperature. The error bars shown at 900 °C are representative for the remaining temperatures. The activation energy displayed in the figure is calculated as an average of the three measurements where $p_{O_2} > 0.008$ atm. The dotted lines are a guide to the eye and have no theoretical significance.

Values of the oxygen ion conductivity have also been calculated from the electrical conductivity relaxation measurements, $\sigma_{O^{2-}}$(ECR), and compared with values of the oxygen ion conductivity from electrical conductivity measurements, $\sigma_{O^{2-}}$(EC). The values of $\sigma_{O^{2-}}$(EC) have been calculated by subtracting the *p*- and *n*-type contribution from the measured electrical conductivity. The values of $\sigma_{O^{2-}}$(ECR) have been calculated as $\sigma_{O^{2-}} = (c_O z_O^2 e^2 D_O)/(k_B T)$, where z_O is the charge number of an oxygen ion. Table 7 shows the oxygen ion conductivity determined with the two methods. It should be noted that $\sigma_{O^{2-}}$(ECR) has been calculated in the p_{O_2}-range of 0.008−0.209 atm where $\delta \approx 0.10$ at 900 °C. The electrical conductivity measurements have been carried out in a region where $\delta \approx 0.213$. Assuming a constant value of D_V, the oxygen ion conductivity is proportional with δ. A corrected value of the oxygen ion conductivity based on the electrical conductivity relaxation measurements, $\sigma_{O^{2-}}(\mathrm{ECR}, \delta = 0.213)$, has thus been calculated and is also displayed in Table 7. $\sigma_{O^{2-}}(\mathrm{ECR}, \delta = 0.213)$ has been calculated as

$$\sigma_{O^{2-}}(\mathrm{ECR}, \delta = 0.213) = \sigma_{O^{2-}}(\mathrm{ECR}) \frac{\delta(\mathrm{EC})}{\delta(\mathrm{ECR})}. \quad (24)$$

δ(ECR) is the average value of δ for the three measurements (δ(ECR) = 0.12) in the p_{O_2}-range of 0.008−0.209 atm at each temperature and δ(EC) = 0.213. Fairly good agreement is observed between ionic conductivity determined by the two methods.

Table 8 shows values and activation energies for the different transport parameters. D_O is the oxygen component diffusion coefficient and is calculated as

Table 7
Oxygen ion conductivity of LSF40 measured from electrical conductivity relaxation $\sigma_{O^{2-}}$(ECR) and electrical conductivity measurements $\sigma_{O^{2-}}$(EC)

T (°C)	$\sigma_{O^{2-}}$ (ECR) (S cm^{-1})	$\sigma_{O^{2-}}$ (EC) (S cm^{-1})	$\sigma_{O^{2-}}$(ECR, $\delta = 0.213$) (S cm^{-1})
900	0.05 ± 0.01	0.25 ± 0.05	0.10 ± 0.01
1000	0.21 ± 0.05	0.44 ± 0.05	0.35 ± 0.05

A corrected value, $\sigma_{O^{2-}}$(ECR, $\delta = 0.213$), of the electrical conductivity measurements corresponding to $\delta = 0.213$ is also shown.

Table 6
Transport parameters measured in this study compared with literature values

Composition	Temperature (°C)	Transport parameter (cm^2 s^{-1})	Value	This study
$La_{0.6}Sr_{0.4}FeO_{3-\delta}$	1000	D_V[a]	1.95×10^{-5} [35]	1.41×10^{-5}
$La_{0.6}Sr_{0.4}FeO_{3-\delta}$	1000	D_V[b]	0.77×10^{-5} [12]	1.41×10^{-5}
$La_{0.6}Sr_{0.4}FeO_{3-\delta}$	950	D_V[c]	1.3×10^{-5} [10]	0.82×10^{-5}
$La_{0.6}Sr_{0.4}FeO_{3-\delta}$	800	D_V[c]	0.60×10^{-5} [10]	0.15×10^{-5}

D_V is the vacancy diffusion coefficient. The values in this study are based on the average value of the three measurements for $p_{O_2} > 0.008$ atm.
[a]Determined from $^{16}O/^{18}O$ isotopic exchange experiments.
[b]Determined from oxygen permeation experiments.
[c]Determined from ECR.

Table 8
Various transport parameters calculated on the basis of data from electrical conductivity relaxation and the oxygen nonstoichiometry data

	800 °C	900 °C	1000 °C	E_A (kJ mol^{-1})
D_{Chem} (cm^2)	0.62×10^{-5}	1.8×10^{-5}	7.1×10^{-5}	137
D_O (cm^2)	0.39×10^{-7}	1.5×10^{-7}	6.2×10^{-7}	157
D^* (cm^2)	0.27×10^{-7}	1.1×10^{-7}	4.3×10^{-7}	157
D_V (cm^2 s^{-1})	0.15×10^{-5}	0.44×10^{-5}	1.4×10^{-5}	129
$\sigma_{O^{2-}}$ (S cm^{-1})	0.013	0.049	0.21	156
$\mu_{O^{2-}}$ (V^{-1} cm^2 s^{-1})	0.084×10^{-5}	0.31×10^{-5}	1.3×10^{-5}	157

Notice that these data are an average of the three measurements at each temperature where $p_{O_2} > 0.008$ atm.

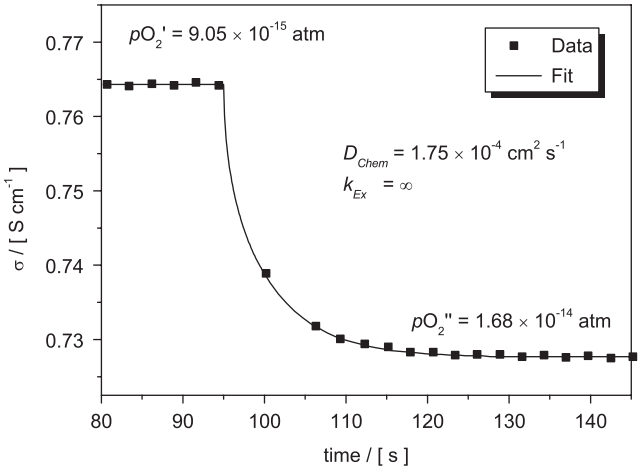

Fig. 9. Fast relaxation in the region where the thermodynamic factor is large (~400), according to Fig. 4. Relevant parameters are displayed in the figure. The data could equally well be fitted with $D_{Chem} = \infty$ and $k_{Ex} = 7.0 \times 10^{-3}$ cm s^{-1}.

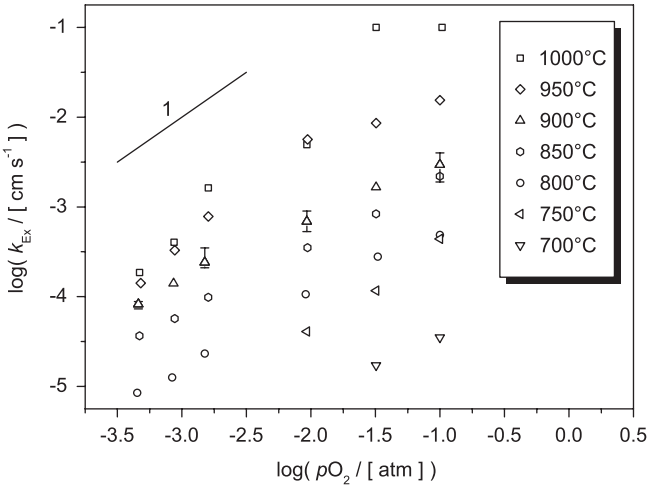

Fig. 10. log(k_{Ex})–log(p_{O_2}) diagram. For 900 °C the error bars are shown. This error bar is typical for temperatures below 900 °C; however, for $T > 900$ °C and $p_{O_2} > 0.004$ the error is significantly larger.

$D_O = D_{Chem}/\gamma$. D^* is the tracer diffusion coefficient and is calculated as $D^* = D_O f$, where f is a correlation factor, which for perovskites approximately equals 0.69 [35]. $\mu_{O^{2-}}$ is the oxygen mobility and is calculated according to $\mu_{O^{2-}} = \sigma_{O^{2-}}/(c_{O^{2-}} ze)$.

4.6. Relaxations for large values of γ

Fig. 9 shows the electrical conductivity as a function of time upon an oxidation at 1000 °C occurring in an $H_2/H_2O/CO_2/CO$ gas mixture (see graph for p_{O_2}-conditions). It is observed that the time before the new equilibrium condition has been reached is extremely short (<30 s). From this relaxation it is possible to extract a minimum value of D_{Chem}. It can with certainty be concluded that $D_{Chem} > 1.75 \times 10^{-4}$ cm^2 s^{-1}. Notice that this value of the chemical diffusion coefficient is approximately twice the value observed at high p_{O_2} (according to Fig. 7 and Table 8). Such fast relaxations can only be accounted for by realizing that the thermodynamic factor in this p_{O_2}-range is significantly larger, by a factor of 2–3, than in the high p_{O_2}-range. We have to notice that the time for changing the gas surrounding the sample is probably of a time scale such that it influences the relaxation. We therefore refer to the measured value of D_{Chem} as a minimum value. The data could equally well be fitted with $D_{Chem} = \infty$ and $k_{Ex} = 7.0 \times 10^{-3}$ cm s^{-1}.

4.7. Oxygen surface exchange

The surface exchange coefficient, k_{Ex}, is shown as a function of log(p_{O_2}) at different temperatures in Fig. 10. The error bars are shown for 900 °C. A line segment with the slope 1 is also given in the figure. For the values where $T > 900$ °C and where $k_{Ex} > 0.004$ cm s^{-1}, the uncertainty is significantly larger than the error bar given for 900 °C. In this region the oxygen incorporation into the sample is governed by diffusion and it thus becomes very difficult to measure k_{Ex} accurately.

Fig. 11 shows k_O as a function of log(p_{O_2}). k_O has been calculated as $k_O = k_{Ex}/\gamma$ [10]. The measured value of γ has been taken from Fig. 4. k_O has therefore only been calculated at 800, 900 and 1000 °C where the thermodynamic factor can be determined accurately. It is observed that k_O decreases with decreasing p_{O_2} and as a first approximation k_{Ex} and k_O can be described using the expressions $k_{Ex} = a p_{O_2}^n$ and $k_O = b p_{O_2}^m$. Table 9 shows values of the best fit to the expression described above.

tenElshof measured n-values in the range of 0.75−0.83. We are, however, skeptical regarding the large n-values at

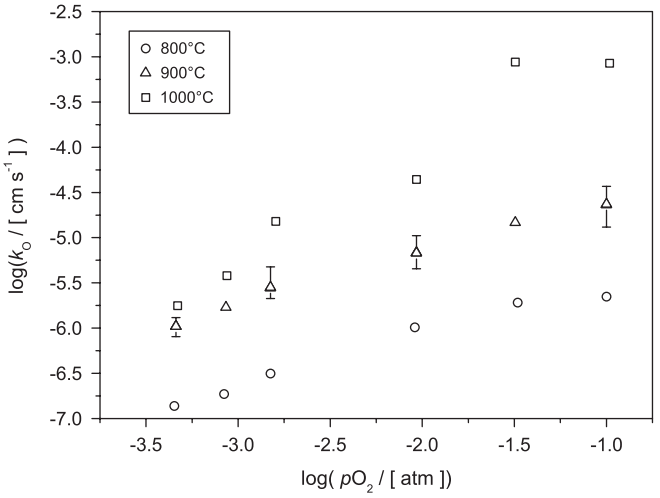

Fig. 11. $\log k_O$–$\log(p_{O_2})$ diagram. For 900 °C the error bars are shown. These error bars are typical for all the other point in the figure.

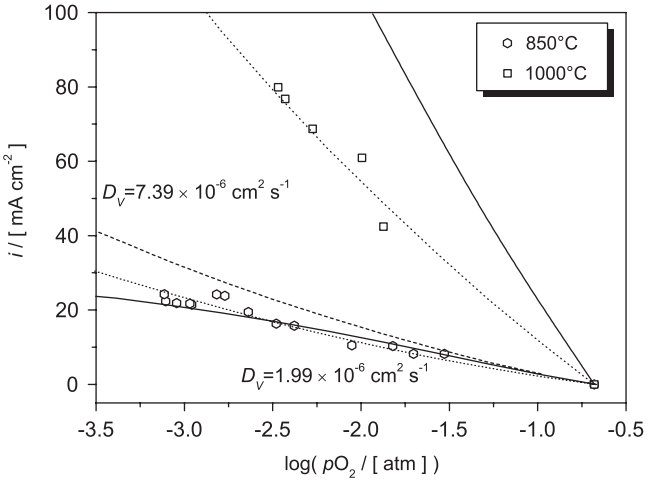

Fig. 12. Current density through a membrane of LSF40 as a function of $\log(p_{O_2})$ at the anode side. Also shown are curves calculated on the basis of the model presented in the Theory section. The dotted lines depicted in the figure correspond to an infinitely fast surface exchange reaction and with the depicted values of D_V. For further details see the text and Table 10.

Table 9
Best fit values of k_{Ex} and k_O to the expressions $k_{Ex} = a\ p_{O_2}{}^n$ and $k_O = b p_{O_2}{}^m$

T (°C)	a (cm s^{-1})	n	b (cm s^{-1})	m
700	1.5×10^{-4}	0.62		
750	6.4×10^{-3}	1.14		
800	3.5×10^{-3}	0.78	1.05×10^{-5}	0.55
850	0.012	0.76		
900	0.015	0.66	9.61×10^{-5}	0.57
950	0.18	0.88		
1000	2.66	1.22	0.22	1.20

Table 10
Values used to calculate the lines displayed in Fig. 12

	D_V (cm^2 s^{-1})	k_O (cm s^{-1})
Solid (850 °C)	2.70×10^{-6}	$5.2 \times 10^{-5} \cdot p_{O_2}{}^{0.56}$
Dotted (850 °C)	1.99×10^{-6}	∞
Dashed (850 °C)	2.70×10^{-6}	∞
Solid (1000 °C)	1.41×10^{-5}	$0.22 \cdot p_{O_2}{}^{1.20}$
Dotted (1000 °C)	7.39×10^{-6}	∞

750 and 1000 °C for our sample, since thin film measurements on LSF40 also have indicated slopes in the range of 0.66−1.03 for k_{Ex} [36].

We have calculated the activation energy for k_{Ex} at $p_{O_2} = 8.7 \times 10^{-4}$ atm to be 199 ± 23 kJ mol^{-1}. For k_O the activation energy is 173 ± 34 kJ mol^{-1} at $p_{O_2} = 8.7 \times 10^{-4}$ atm. tenElshof et al. [10] found an activation energy of 131 ± 14 kJ mol^{-1} for k_O. At 800 °C we measure the same values of k_{Ex} as tenElshof, but at higher temperatures, the values measured in this study are significantly higher. The larger activation energy of k_{Ex} than for D_{Chem} shows that, when going to lower temperature, surface exchange will become the limiting process for oxygen exchange.

4.8. Oxygen transport through a dense membrane

Oxygen permeation measurements were carried out on a membrane of LSF40 with a thickness of 1.34 mm. Air was applied on the cathode side of the membrane. On the anode side of the membrane, mixtures of nitrogen and oxygen were applied. After these measurements the membrane was tested with $H_2/H_2O/N_2$ on the anode SIDE.

Fig. 12 shows the equivalent electrical current density i through the membrane as a function of the downstream $\log(p_{O_2})$. It is observed that when decreasing the p_{O_2} on the low-p_{O_2} side the oxygen flux increases. An increase in temperature at a constant p_{O_2} also increases the flux through the membrane, which is attributed to an increase in the vacancy diffusion coefficient and an increase in the oxygen nonstoichiometry. The lines are calculated using Eqs. (16)–(19).

Due to the difference in the magnitude of flux at 850 and 1000 °C and the difference in the predicted fluxes, we discuss these results separately.

4.8.1. Oxygen permeation at 850 °C

The solid line which goes through the data points at 850 °C (Fig. 12) has been calculated using an interpolated value of the vacancy diffusion coefficient (data in Table 8) and an interpolated value of k_O (data from Table 9). The oxygen nonstoichiometry data have been calculated using the values in Table 4. The solid line describes the measured data with good accuracy. Table 10 shows the values used for calculating the three curves in the figure. Assuming an infinitely fast surface exchange coefficient on both sides of

the membrane, the data at 850 °C could be fitted well with $D_V = 1.99 \times 10^{-6}\,cm^2\,s^{-1}$ (dotted line). An infinitely fast surface exchange coefficient and $D_V = 2.70 \times 10^{-6}\,cm^2\,s^{-1}$ give the dashed line in Fig. 12.

4.8.2. *Oxygen permeation at* 1000 °C

The solid line in Fig. 12 shows the calculated flux using the oxygen nonstoichiometry data (third degree polynomial fit to the actual measurements), the measured vacancy diffusion coefficient and the surface exchange coefficient displayed in Table 9. The measured flux is thus significantly smaller (by a factor of ~2 over the measured p_{O_2}-range) than the calculated flux. The oxygen permeation fluxes could be fitted well with $D_V = 7.39 \times 10^{-6}\,cm^2\,s^{-1}$ (dotted line in Fig. 12). This value must represent a minimum value of D_V. The vacancy diffusion coefficient determined from oxygen permeation values is thus lower by a factor of 1.9 than the value determined from electrical conductivity relaxation measurements. From data by tenElshof [10,12] the same tendency and similar values can be found (these data are also displayed in Table 6). The reason for measuring a smaller vacancy diffusion coefficient in an oxygen permeation experiment is at present unclear. In the permeation experiment leaks would increase the oxygen flux thereby resulting in a larger value of the vacancy diffusion coefficient. The uncertainty on the vacancy diffusion coefficient is estimated to be approximately ±20% which originates mainly from the uncertainty on the absolute oxygen nonstoichiometry. A shift in the absolute oxygen nonstoichiometry of $\Delta\delta = -0.015$ increases the fitted vacancy diffusion coefficient to $D_V = 8.40 \times 10^{-6}\,cm^2\,s^{-1}$ (increase of 14%). It should be noted that the density of the sample used for the oxygen permeation measurements (95% of the theoretical value) is larger than the density used for the electrical conductivity relaxation measurements (92% of the theoretical value). In addition, the synthesis of the two samples was not identical. Differences in the synthesis method can also lead to different values of the oxygen permeation as shown by Qi et al. [37].

Several measurements were also performed in $H_2/H_2O/N_2$ mixtures. Table 11 shows measured values of the current density, i_{Meas}, as a function of the p_{O_2} on the anode side. At 1000 °C the measured current density is observed to be approximately 10 times larger than what was measured in the oxygen/nitrogen regime (Fig. 12). This is attributed to the larger driving force over the membrane. When decreasing the temperature the current density also decreases. When increasing the driving force (decreasing p''_{O_2}) the flux is expected to increase. This is observed at 900 °C; however, the uncertainty on the measurements is fairly large and this is most likely the origin for the data not showing this trend at 800 and 1000 °C.

Using ambipolar diffusion theory (Eq. (12)), current densities based on δ and D_{Chem} measurements have been calculated, i_{Calc}. These values are also displayed in Table 11. When using the ambipolar conductivity instead of the oxygen ion conductivity, the flux decreases with approximately 13% at 1000 °C when being at a p''_{O_2} lower than the *pn*-transition. The *n*-type contribution to the electrical conductivity at 800 °C has been calculated from the band gap as described in Section 4.4, since no electrical conductivity measurements were carried out at this temperature and at these low p_{O_2}.

From Table 11 it is observed that the calculated current density is larger than the measured by an average of 15%. Part of this can be ascribed to a surface exchange reaction, which is not accounted for in this model, but also effects like vacancy ordering will decrease the measured current densities.

When including the surface exchange reaction on the cathode side of the membrane at 800 °C and $p''_{O_2} = 3.63 \times 10^{-19}$ atm the flux decreases to 189 mA cm^{-2}, a reduction of 8%. Decreasing the membrane thickness to 100 μm at the same temperature and p_{O_2}, the flux is (without surface exchange reactions) 2.77 A cm^{-2}. Including the surface exchange reaction the flux decreases to

Table 11
Measured values of the current density, i_{Meas}, compared with calculated values, i_{Calc}

T (°C)	p''_{O_2} (atm)	i_{Meas} (mA cm^{-2})	D_V (cm^2 s^{-1})	i_{Calc} (mA cm^{-2})	$\frac{i_{Calc} - i_{Meas}}{i_{Meas}}$ (%)
1000	7.23×10^{-14}	671	7.39×10^{-6}	732	9.1
1003	3.36×10^{-14}	664	7.39×10^{-6}	752	13.3
1004	1.74×10^{-14}	681	7.39×10^{-6}	761	11.7
900	5.15×10^{-16}	411	4.37×10^{-6}	498	21.2
900	3.21×10^{-16}	433	4.37×10^{-6}	505	16.6
900	1.44×10^{-16}	435	4.37×10^{-6}	516	18.6
800	1.80×10^{-18}	199	1.46×10^{-6}	198	−0.5
800	1.01×10^{-18}	165	1.46×10^{-6}	201	21.8
800	3.63×10^{-19}	165	1.46×10^{-6}	206	24.8

All measurements were carried out with air on the cathode side ($p'_{O_2} = 0.209$ atm). p''_{O_2} is the oxygen partial pressure on the low-p_{O_2} side. i_{Meas} and i_{Calc} are the measured and calculated current density, respectively.

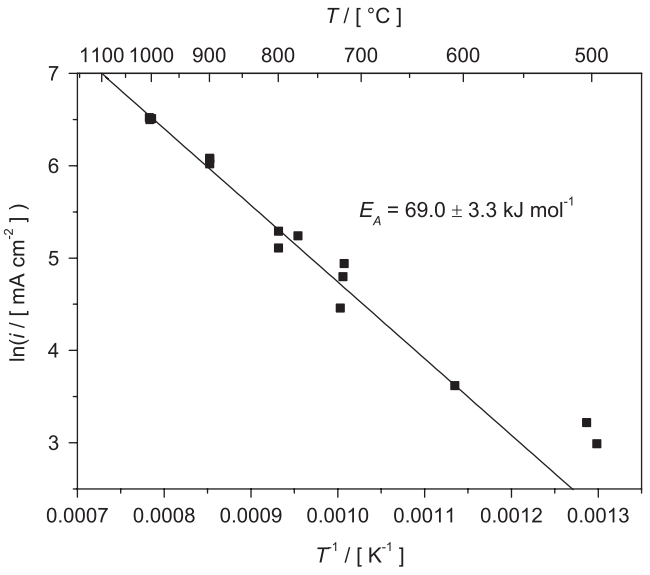

Fig. 13. Arrhenius-type plot showing the natural logarithm of the flux versus the reciprocal absolute temperature. The activation energy is shown in the figure.

$0.93\,A\,cm^{-2}$, a reduction of 66%. For a thin film membrane the total loss in driving force over the membrane is thus mainly found over the cathode side of the membrane. It should be noted that k_O was derived from electrical conductivity relaxation. In these types of experiments the sample is only subjected to small perturbations in the oxygen partial pressure across the interface. The maximum current density in the electrical conductivity relaxation experiments performed in this study is of the order of $10-20\,mA\,cm^{-2}$. However, in the membrane experiment, the current density is of the order of $150-700\,mA\,cm^{-2}$ causing the assumption of a small perturbation to be very questionable.

Fig. 13 shows the natural logarithm of the current density as a function of the reciprocal absolute temperature. The slope corresponds to an activation energy of $69.0 \pm 3.3\,kJ\,mol^{-1}$. The activation energy of the flux is significantly smaller than the activation energy of the transport parameters listed in Table 8. This can be accounted for by realizing that according to the $H_2O/H_2/O_2$ equilibrium a decrease in temperature decreases the p_{O_2}, thus increasing the driving force across the membrane. At approximately 500 °C the current density levels off which is attributed to a leak of approximately $10\,mA\,cm^{-2}$.

Upon disassembling the membrane reactor it was observed that the membrane had cracked into many small pieces. We have previously observed that it is possible to do a thermal cycle with a membrane (different composition) which has not been subjected to such a p_{O_2}-gradient. The disintegration of the membrane is due to stress that arises due to chemical expansion. That is, the gradient in the oxygen ion vacancy concentration in the membrane material gives rise to a significant stress, which causes the destruction of the membrane.

5. Conclusion

Here, we have investigated and analyzed properties of the composition $(La_{0.6}Sr_{0.4})_{0.99}FeO_{3-\delta}$.

The oxygen nonstoichiometry as a function of the temperature and p_{O_2} has been determined using thermogravimetry. A large region where the oxygen nonstoichiometry was constant as a function of p_{O_2} was found. This region was attributed to electronic stoichiometry.

The electrical conductivity, σ, was determined in the high-temperature region (700−1000 °C) and under varying oxygen partial pressures. A *pn*-transition was found when going to reducing conditions. Correlating the electrical conductivity with values of the concentration of tetravalent iron, it was observed that the electrical conductivity was almost solely determined by the concentration of charge carriers and not the temperature. The mobility of the electron holes decreased with increasing oxygen vacancy concentration (from $0.2\,cm^2\,V^{-1}s^{-1}$ ($\delta = 0.06$) to $0.1\,cm^2\,V^{-1}\,s^{-1}$ ($\delta = 0.16$)). Similar values and tendencies have been observed by Patrakeev et al. [4].

Using electrical conductivity relaxation, values of the chemical diffusion coefficient, D_{Chem}, and the surface exchange coefficient, k_{Ex}, have been determined. At 800 °C D_{Chem} was found to be $D_{Chem} = 6.2 \times 10^{-6}\,cm^2\,s^{-1}$. The activation energy of D_{Chem} has been calculated to be $137\,kJ\,mol^{-1}$. k_{Ex} was found to decrease with decreasing p_{O_2}.

Oxygen permeation measurements were carried out on a membrane disk with air on the cathode side and nitrogen/air mixtures and wet nitrogen/hydrogen mixtures on the anode side. It was found that at 850 °C in nitrogen/air mixtures, the oxygen nonstoichiometry measurements in combination with the oxygen transport properties could describe the observed flux. Measurements in wet hydrogen/nitrogen yielded high oxygen fluxes e.g. $J_{O_2} \approx 1.8 \times 10^{-6}\,mol\,cm^{-2}\,s^{-1}$ (corresponding to an equivalent electrical current of $670\,mA\,cm^{-2}$). From model calculations it was estimated that the oxygen permeation under very reducing conditions is determined by a combination of the surface exchange coefficient on the air side of the membrane and the ambipolar conductivity. It is interesting to note that when the fundamental properties such as the oxygen nonstoichiometry and the electronic and ionic transport properties are known, the oxygen permeation under a large oxygen flux can be calculated with an accuracy within 15%. Upon disassembling the membrane reactor it was observed that the membrane had cracked into many small pieces which was attributed to chemical expansion.

Acknowledgments

M. Solvang and B.H. Simonsen are acknowledged for their assistance in the dilatometry experiment. J.V.T. Høgh is acknowledged for help with the oxygen permeation experiment. M. Menon is acknowledged for valuable comments and careful proof reading of the paper.

References

[1] H.L. Lein, O.S. Andersen, P.E. Vullum, E. Lara-Curzio, R. Holmestad, M.A. Einarsrud, T. Grande, J. Solid State Electrochem. 10 (2006) 635–642.
[2] J. Mizusaki, M. Yoshihiro, S. Yamauchi, K. Fueki, J. Solid State Chem. 58 (1985) 257–266.
[3] E. Bucher, W. Sitte, J. Electroceram. 13 (2004) 779–784.
[4] M.V. Patrakeev, I.A. Leonidov, V.L. Kozhevnikov, K.R. Poeppelmeier, J. Solid State Chem. 178 (2005) 921–927.
[5] I. Wærnhus, P.E. Vullum, R. Holmestad, T. Grande, K. Wiik, Solid State Ionics 176 (2005) 2783–2790.
[6] I. Wærnhus, T. Grande, K. Wiik, Solid State Ionics 176 (2005) 2609–2616.
[7] M.V. Patrakeev, J.A. Bahteeva, E.B. Mitberg, I.A. Leonidova, V.L. Kozhevnikov, K.R. Poeppelmeier, J. Solid State Chem. 172 (2003) 219–231.
[8] J. Mizusaki, T. Sasamoto, W.R. Cannon, H.K. Bowen, J. Am. Ceram. Soc. 66 (1983) 247–252.
[9] X.D. Zhou, Q. Cai, J. Yang, M. Kim, W.B. Yelon, W.J. James, Y.W. Shin, B.J. Scarfino, H.U. Anderson, J. Appl. Phys. 97 (2005) 10C314.
[10] J.E. tenElshof, M.H.R. Lankhorst, H.J.M. Bouwmeester, J. Electrochem. Soc. 144 (1997) 1060–1067.
[11] J. Yoo, A. Verma, S.Y. Wang, A.J. Jacobson, J. Electrochem. Soc. 152 (2005) A497–A505.
[12] J.E. tenElshof, H.J.M. Bouwmeester, H. Verweij, Solid State Ionics 81 (1995) 97–109.
[13] M. Søgaard, P.V. Hendriksen, F.W. Poulsen, M. Mogensen, J. Electroceram. 13 (2004) 811–816.
[14] R. Glenne, Ph.D. Thesis, Norwegian University of Science and Technology, Trondheim, 2001.
[15] I. Yasuda, M. Hishinuma, Solid State Ionics 80 (1995) 141–150.
[16] I. Yasuda, M. Hishinuma, J. Solid State Chem. 123 (1996) 382–390.
[17] C.R. Song, H.I. Yoo, Solid State Ionics 124 (1999) 289–299.
[18] H.S. Carslaw, J.C. Jaeger, Conduction of Heat in Solids, second ed., Clarendon Press, Oxford, 1959.
[19] J.R. Hansen, Ph.D. Thesis, Risø National Laboratory, Denmark, 2000.
[20] M. Søgaard, P.V. Hendriksen, F.W. Poulsen, in: Proceedings of the 26th Risø International Symposium on Material Science, 2005.
[21] H.J.M. Bouwmeester, A.J. Burggraaf, in: H.J.M. Bouwmeester, P.J. Gellings (Eds.), The CRC Handbook of Solid State Electrochemistry, CRC Press, Boca Raton, FL, 1997, pp. 481–553.
[22] P.V. Hendriksen, P.H. Larsen, M. Mogensen, F.W. Poulsen, K. Wiik, Catal. Today 56 (2000) 283–295.
[23] C. Wagner, Prog. Solid State Chem. 10 (1975) 3–16.
[24] K. Lade, T. Jacobsen, Solid State Ionics 72 (1994) 218–223.
[25] L.A. Chick, L.R. Pederson, G.D. Maupin, J.L. Bates, L.E. Thomas, G.J. Exarhos, Mater. Lett. 10 (1990) 6–12.
[26] S.J. Benson, Ph.D. Thesis, Imperial College, London, 1999.
[27] K.K. Hansen, E.M. Skou, H. Christensen, T. Turek, J. Catal. 199 (2001) 132–140.
[28] J. Crank, The Mathematics of Diffusion, Clarendon Press, Oxford, 1979.
[29] S.E. Dann, D.B. Currie, M.T. Weller, M.F. Thomas, A.D. Alrawwas, J. Solid State Chem. 109 (1994) 134–144.
[30] A. Fossdal, Ph.D. Thesis, Norwegian University of Science and Technology, Trondheim, 2003.
[31] S.B. Adler, J. Am. Ceram. Soc. 84 (2001) 2117–2119.
[32] A. Fossdal, M. Menon, I. Wærnhus, K. Wiik, M.A. Einarsrud, T. Grande, J. Am. Ceram. Soc. 87 (2004) 1952–1958.
[33] M. Søgaard, P.V. Hendriksen, F.W. Poulsen, M. Mogensen, E. Skou, Solid State Ionics 177 (2006) 3285–3296.
[34] H.L. Tuller, in: O.T. Sørensen (Ed.), Nonstoichiometric Oxides, Academic Press, New York, 1981, pp. 271–335.
[35] T. Ishigaki, S. Yamauchi, K. Kishio, J. Mizusaki, K. Fueki, J. Solid State Chem. 73 (1988) 179–187.
[36] M. Søgaard, Ph.D. Thesis, Risø National Laboratory, Denmark, 2005.
[37] X. Qi, Y.S. Lin, S.L. Swartz, Ind. Eng. Chem. Res. 39 (2000) 646–653.